machines

MDPI

Article

Effect of Purge on Secondary Flows in Turbine Due to Interaction Between Cavity Flow and Main Channel

Daniele Biassoni *, Dario Barsi and Davide Lengani

Department of Mechanical, Energy, Management, and Transportation Engineering (DIME), University of Genova, Via All'Opera Pia 15, 16145 Genova, Italy; dario.barsi@unige.it (D.B.); davide.lengani@edu.unige.it (D.L.)
* Correspondence: daniele.biassoni@edu.unige.it

Abstract: Nowadays, a lot of efforts are being made to increase turbine inlet temperatures (TIT), with the aim of increasing efficiency in aircraft and power generation turbines. Due to the higher temperature level, advanced cooling solutions to preserve material durability are necessary. It is essential to avoid contact between hot gases and the temperature-sensitive components, such as the stator and rotor cavity disks. Modern gas turbine performance optimization centers on reducing leakage and refining sealing systems. The interaction between the main flow and cavity flow in stator/rotor systems has a significant role in loss generation. This study employs Unsteady Reynolds-Averaged Navier–Stokes (URANS) simulations to investigate the unsteady interactions within the stator/rotor cavity of a low-pressure turbine. Numerical results are compared and validated against experimental data obtained in the cavity rig of the University of Genova. The research focuses on the effects of stator/rotor interactions, including wake ingestion from upstream rotor bars and the blocking influence of downstream potential effects on cavity sealing effectiveness. In this paper, a comparison between the zero cooling air flow rate and cavity sealing condition is shown. Special attention is given to unsteady loss mechanisms occurring downstream of the vane row and in areas where the cavity flow re-enters the main channel, showing how cooling flow rates affect these losses. From this study, it can be seen that by increasing the cooling flow rate injected into the cavity, there is an increase in the hub's passage vortex effect and there is a more intense interaction between the main flow and the cavity flow. These results offer valuable insights into the mechanisms of interaction between the main flow and cavity flow.

Keywords: axial flow turbine; cavity/mean-flow interaction; CFD; rim seal

check for updates

Academic Editor: Davide Astolfi

Received: 23 December 2024
Revised: 17 January 2025
Accepted: 21 January 2025
Published: 22 January 2025

Citation: Biassoni, D.; Barsi, D.; Lengani, D. Effect of Purge on Secondary Flows in Turbine Due to Interaction Between Cavity Flow and Main Channel. *Machines* **2025**, *13*, 77. https://doi.org/10.3390/machines13020077

Copyright: © 2025 by the authors. Licensee MDPI, Basel, Switzerland. This article is an open access article distributed under the terms and conditions of the Creative Commons Attribution (CC BY) license (https://creativecommons.org/licenses/by/4.0/).

1. Introduction

In recent decades, turbine inlet temperatures (TIT) in gas turbines have risen by approximately 3 degrees annually to enhance efficiency. This increase has been supported by advancements in materials capable of enduring extreme stresses and temperatures, as well as the development of secondary air systems. These systems play a vital role in cooling components like blades and cavity disks that are not designed for high-temperature exposure. Without effective secondary air systems, hot gas ingestion into cavities would significantly elevate component temperatures, drastically reducing their lifespan. Consequently, sealing cavities through secondary air systems is essential, though minimizing the required sealing flow presents significant challenges for turbine designers. Notably, Moore [1] estimated that a 1% reduction in sealing purge flow could improve specific fuel consumption by 0.4%, thereby increasing efficiency.

Due to reaching of the performance limits of turbines, materials are subjected to greater mechanical and thermal stresses. Secondary air systems are indispensable for cooling, maintaining pressure balance on bearings, isolating the oil system, and preventing hot gas ingestion. Theoretical studies of hot gas ingestion, beginning with Johnson [2] and further expanded by Chew et al. [3], have identified mechanisms governing this phenomenon, including disk pumping, pressure-driven ingestion, combined effects, rim seal geometry, turbulent transport, flow entrainment, density ratios, eccentricity, and unsteady flow interactions.

Since the 1970s, researchers have aimed to supplement experimental test rigs with numerical simulations and mathematical models to predict gas flow into rotor-disk cavities. However, the complex, interrelated factors of ingestion phenomena challenge simplified models, particularly given the variations in cavity and main channel geometries.

Additionally, secondary air injection, used for cavity cooling and sealing, influences leakage flow behavior. Schrewe et al. [4] demonstrated that seal air outflow significantly interacts with vane and blade row flows, altering downstream blade incidence angles. Similar trends in high-pressure turbines have been observed by Ong et al. [5], Zerobin et al. [6], Sterzinger et al. [7], and Schuepbach et al. [8]. Chilla et al. [9] highlighted how rim seal flow influences the turbine hub boundary layer. This unsteady interaction depends on the potential pressure field of the downstream rotor and Kelvin–Helmholtz instabilities within the cavity. Jackson et al. [10,11] studied with experimental and numerical data the influence of swirl on losses in a low-pressure turbine stator-well cavity. They found that the pre-swirled superposed flows reduce the ingestion of negatively swirling fluid, increasing the cavity swirl ratio and reducing losses. Under the design conditions, sealing effectiveness improved with higher superposed flow rates. More recently, a new test rig has been designed [12] at the University of Florence to analyze the issue of high-pressure turbine main annulus flow ingestion into wheel spaces. The rig is equipped with advanced optical measurement techniques, which have been validated [13] and utilized to assess the impact of the density ratio on rim sealing effectiveness [14]. The unsteadiness of ingestion phenomena has limited the applicability of stationary CFD methods, leading to the adoption of unsteady approaches, such as URANS and LES. While the RANS methods offer limited accuracy, LES (high-fidelity simulations) provide detailed results at significant computational expense; for this reason, they are not readily practicable for real cases. The intent is to trace useful global indications with a low fidelity simulation. URANS methods strike a practical balance between computational cost and result reliability, though with the limitation of reduced resolution of vortex structures. Several studies, such as those by Cao et al. [15], Roy et al. [16], Beard et al. [17], Savov and Atkins [18], Schadler et al. [19], Town et al. [20], Revert et al. [21], and Hu et al. [22], have highlighted the role of cavity geometry and disk pumping effects in driving unsteady cavity flow behavior.

At the Aerodynamics and Turbomachinery Laboratory of the University of Genoa, a low-pressure turbine (LPT) experimental test rig has been developed to replicate real cavity geometries and simulate cavity-main flow interactions under realistic conditions [23]. The rig uses a stator-induced pressure gradient to drive cavity flow and incorporates rotating bars to reproduce wake effects from upstream rotors and potential flow effects from downstream rotors. These experimental studies have focused on characterizing the main flow interactions in the cavity and provided valuable data for validating numerical simulations [24,25]. Further numerical studies have primarily aimed at estimating loss mechanisms and evaluating the effects of cooling flow injection on cavity sealing performance [26,27].

The present work extends these previous analyses to the unsteady characteristics of cavity flow under two extreme cooling flow rates condition: zero cooling injected into

the cavity and complete sealing of the cavity. The aim is to determine how cooling flow variations influence the cavity-main flow interactions and overall system performance, with particular attention to conditions downstream of the vane and their impact on the rotor row inlet flow. The novelty of the present paper lies in the detailed analysis of the radial and tangential displacement of loss cores, as well as the influence of wake ingestion and downstream potential effects on cavity sealing effectiveness. Furthermore, the study highlights how increasing cooling flow rates intensifies hub passage vortex interactions, modifying the secondary flow pattern in ways not previously quantified. These findings contribute to a deeper understanding of turbine performance optimization, particularly in leakage minimization and sealing strategies.

2. Methods

2.1. Experimental Test Rig

The annular low-pressure axial flow turbine utilized in this study is housed in the Aerodynamics and Turbomachinery Laboratory at the University of Genova. This experimental setup includes a main flow channel and an axisymmetric cavity located below the vane. The test rig is designed to closely replicate the geometry of a low-pressure turbine stage used in aircraft engines, employing a scaled ratio of 1.5:1. This scaling facilitates detailed experimental measurements and improves spatial resolution. The main channel comprises four rows, with the first being a pre-distributor vane used to set a desired swirl.

Following the pre-distributor vane, a rotating row of small-diameter bars replicates the wakes generated by rotor blades upstream of the main vane. The main vane row accurately reproduces the geometry of a low-pressure turbine (LPT) vane used in aircraft applications. Downstream of the vane, a rotating row of large-diameter bars is included to emulate the potential flow effects induced by rotor blades downstream of the vane. The design of these rotating bars follows the methodology proposed by Opoka and Hodson [28].

The vane has a chord length of 59 mm, with an aspect ratio of 1 and a hub pitch-to-chord ratio of 0.66. The rig's configuration uses a specific number of stator and rotor blades to simplify the geometry for numerical simulations. The stationary rows consist of 84 vanes, while the rotor rows include 63 blades, giving a rotor-to-stator blade count ratio of 4:3. Figure 1 depicts the computational domain used for numerical simulations.

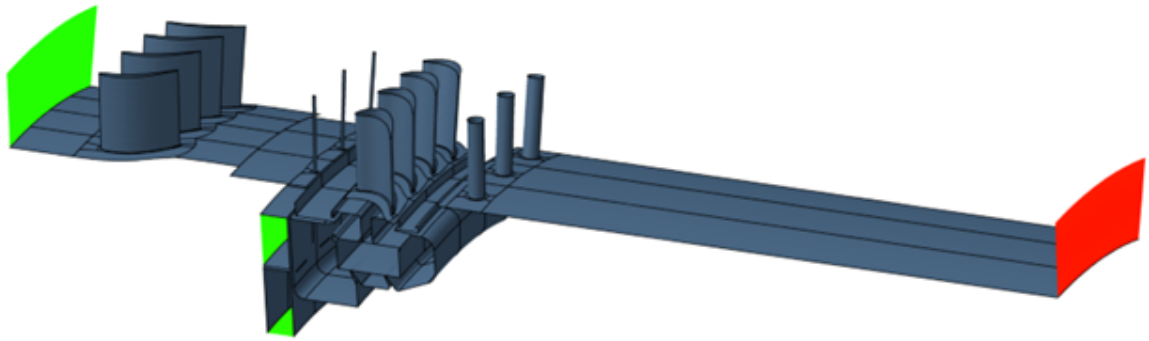


Figure 1. 3D representation of the simulated geometry. Green sections correspond to inlets, while the red section correspond to test rig outlet.

The cavity incorporates two distinct sets of tangentially staggered periodic slots for cooling flow injection. These slots are aligned with the periodicity of the rotor rows. Figure 2 provides a simplified meridional view of the test section and a cross-section showing the cooling slots.

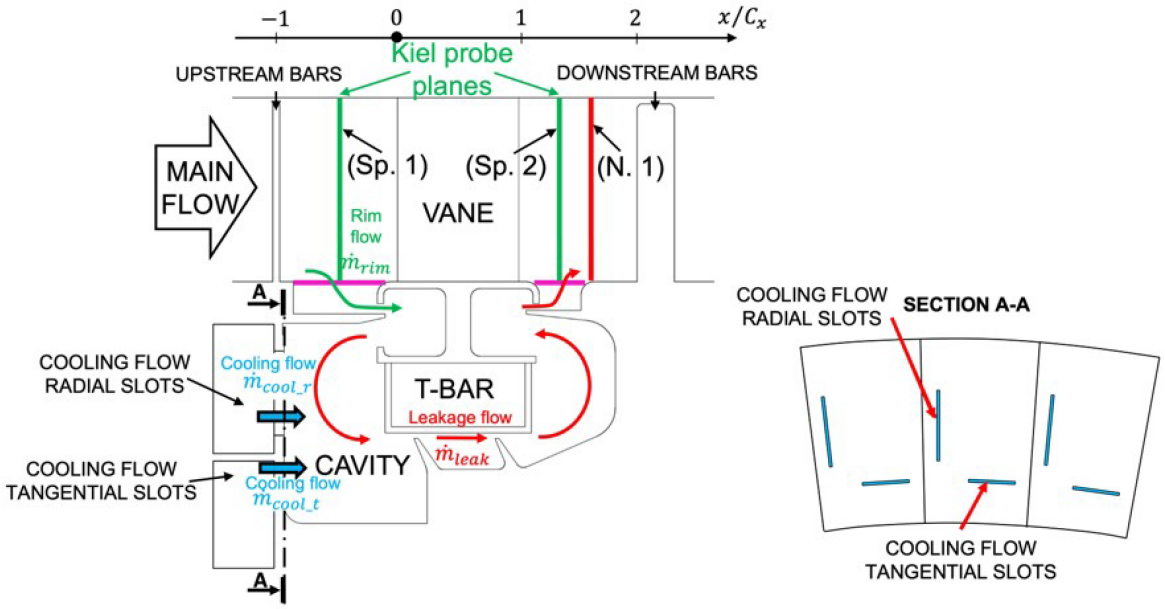


Figure 2. Simplified meridional view of the test section and cross-section showing the cooling slots.

In the main flow path, measurement planes known as "Kiel probe planes" are positioned 0.4 axial chords (C_x) upstream of the vane's leading edge and 0.4 C_x downstream of the trailing edge. These planes indicate the locations where total pressure measurements were carried out using Kiel probes during the experiments. The probes align axially with the cavity inlet and outlet slot centerlines.

The experimental data collected from this setup include pressure distributions within the cavity, total pressure measurements upstream and downstream of the vane, and estimates of cavity leakage flow under various operational conditions. These datasets serve as essential benchmarks for validating Computational Fluid Dynamics (CFD) results. In particular, the experimental total pressure loss coefficient, which has a relative uncertainty of 3%, is considered here. For all simulated cases, the main channel inlet flow rate is fixed at 3.02 kg/s, corresponding to a Reynolds number of approximately 100,000 based on the axial velocity at the vane exit and the axial length of the cavity. The rotational speed is set at 300 rpm, yielding a Rossby number of 0.7. Additional details about the experimental test rig, the instrumentation and measurement uncertainty are available in the work of Guida et al. [23].

2.2. Numerical Simulations

The experimental rig features a rotor-to-stator blade count ratio of 4:3, enabling the use of a reduced computational domain without requiring approximations typical of domain scaling techniques. For Unsteady Reynolds-Averaged Navier–Stokes (URANS) simulations, meshes were generated using Cadence's HexpressOPEN module [29]. The blade passage and cavity system meshes were created separately, with the main channel mesh initially constructed in Autogrid, Cadence's structured mesh generator designed for turbomachinery rows. This employed an O-4-H mesh topology to resolve the four rows of the main channel. Conversely, the cavity and auxiliary domains, essential for imposing cooling slot inlet boundary conditions, were meshed using HexpressOPEN, an unstructured mesh generator.

A y^+ value of 1 was imposed on all surfaces to define the height of the first cell in the main channel and cavity domains. The complete mesh, comprising the main channel, cavity, and cooling slot domains, was assembled within HexpressOPEN. Interface surfaces between the main channel and the cavity were modeled as full non-matching

boundaries and modified into rotor/stator interfaces to apply rotation within the cavity's computational domain.

A grid sensitivity analysis was performed using three different grids with an increasing number of elements. To assess the solution's grid dependency, the percentage ratio of the leakage mass flow rate through the cavity ($\dot{m}_{leak}$) to that through the main channel ($\dot{m}_{FP}$) was used as the test variable. The results obtained are reported in Table 1. The intermediate mesh was selected as seen in a previous study by Barsi et al. [25]. The selected mesh included approximately 35 million nodes for URANS simulations, distributed as 15 million cells for the main channel and 20 million cells for the cavity domain. A multiblock approach was used, incorporating coarser meshes to accelerate the convergence process. Figure 3 illustrates the mesh representation for the entire domain. Figure 4 shows a blade-to-blade view of the the main channel mesh and Figure 5 shows the mesh of the cavity domain only.

Table 1. Grid sensitivity analysis.

	Grid 1	**Grid 2**	**Grid 3**	**Target**
Nodes (millions)	26.5	35	44	Exp
$\dot{m}_{leak}/\dot{m}_{FP}$ (%)	2.120	2.133	2.135	2.297

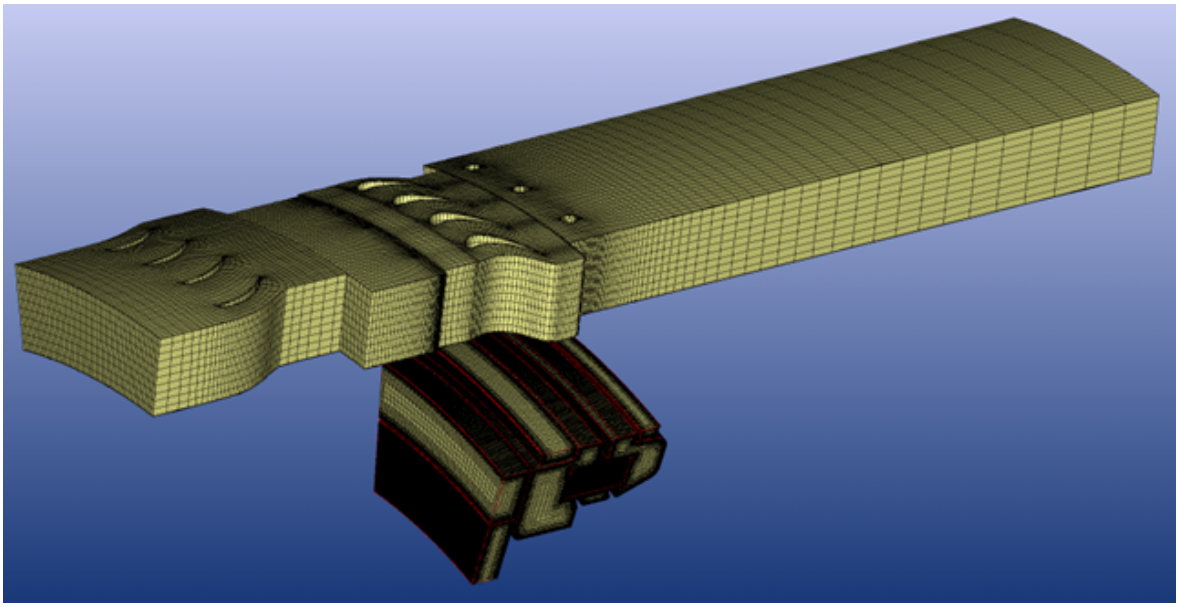


Figure 3. Mesh representation for the entire domain.

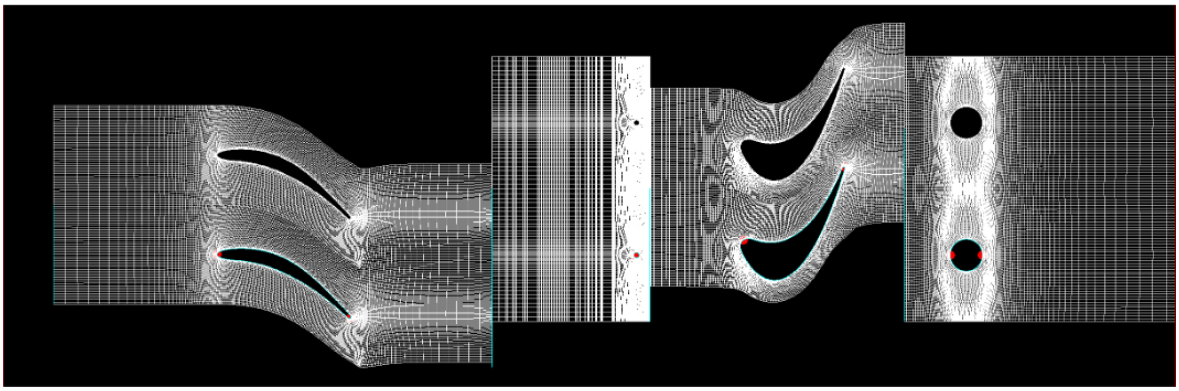


Figure 4. Blade-to-blade representation for the main channel mesh.

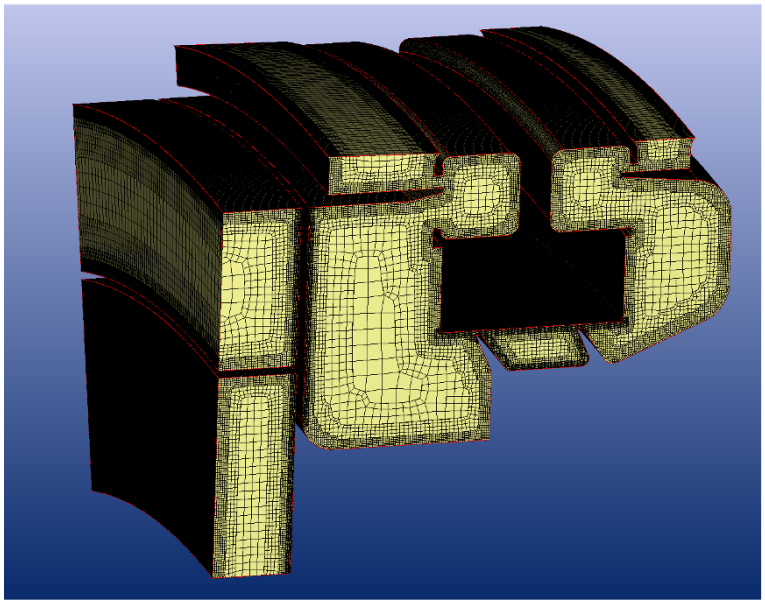


Figure 5. Mesh representation for the cavity domain.

Spatial discretization employed a second-order cell-centered finite volume method, incorporating second- and fourth-order artificial dissipation terms as described by Jameson et al. [30] and Mavriplis et al. [31]. Time discretization utilized a four-stage Runge–Kutta scheme with local time-stepping, enhanced by implicit residual smoothing, dual time-stepping, and a full multigrid approach for convergence acceleration.

Boundary conditions were imposed as follows:

- Inlet Section: Located 6 axial chords (C_x) upstream of the vane:
  - the mass flow rate;
  - static temperature;
  - flow direction (normal to the boundary).
- Outlet Section: Positioned 12 C_x downstream of the vane trailing edge:
  - a static pressure value was imposed.
- Solid Walls: A no-slip condition was applied to all solid surfaces.
- Rotating Components: Rotational boundary conditions corresponding to the nominal rotational speed were applied to surfaces such as:
  - the hub;
  - the rotating bars;
  - the cavity exterior.
- Cooling Domains: Cooling mass flow rate and turbulence parameters were prescribed at the inlet sections, shown in green in Figure 1.

Details of the boundary conditions and operating parameters are summarized in Table 2.

The computational domain included three blade passages and four vane passages. Cadence FineOpen solver was used for the simulations to solve the Navier–Stokes equations. The workstation used for the simulations is equipped with 96 Intel Xeon(R) Platinum 8160 CPUs, each operating at a core frequency of 2.10 GHz. The simulations were performed using 62 CPUs in parallel. The simulations covered 80 angular positions (which corresponds to a computational time-step of 1.2×10^{-4} s) with 30 sub-iterations for each time step in the dual time-stepping approach. Six bar-passing periods, equivalent to 480 time steps, were computed to achieve a periodic solution. This phase required ap-

proximately five days of computation, followed by one day for data sampling and storage. Residual flow rates at the end of the simulation stabilized at approximately 0.3%.

Table 2. Boundary conditions and operating parameters.

B.C.	Quantity	Value
FP inlet	Mass flow rate [kg/s]	3.02
	Static temperature [K]	293
	Flow direction	Normal
	k [m^2/s^2]	13
	ϵ [m^2/s^3]	2000
FP outlet	Static pressure [Pa]	90,000
CS inlet	Mass flow rate [kg/s]	0–2.7% $\dot{m}_{FP}$
	Static temperature [K]	293
	Flow direction	Normal
	k [m^2/s^2]	13
	ϵ [m^2/s^3]	2000
Rotation	Rotational speed [rpm]	300

Turbulence modeling was previously evaluated by the authors [26], using leakage mass flow rates and rim mass flow rates as test variables:

$$\dot{m}_{rim} = \dot{m}_{leak} - \dot{m}_{cool} \quad (1)$$

From this analysis, conducted at four cooling mass flow rate values, the k-ω SST model was selected for its better consistency with the experimental results.

3. Results and Discussion

A comparison between experimental and numerical data is conducted first to validate the CFD procedure. To assess the impact of varying cooling flow rates on vane performance, time-averaged total pressure distributions were evaluated both within and outside the cavity. Figure 6 presents the total pressure loss coefficient (Cpt) distributions for different cooling flow rates, as predicted by the URANS simulations. Experimental results are included for comparison. The diagrams on the right-hand side depict the case of complete sealing (MC = 2.7%). Data were extracted along the green plane (downstream of the vane, Sp. 2) identified in Figure 2, which corresponds to the experimental sampling plane.

Overall, the URANS simulations display:

- Slightly higher peak loss values (red loss cores in the figures);
- Higher Cpt values in the potential flow regions (blue areas) when compared to experimental data;
- Despite these quantitative differences, both URANS predictions and experimental results exhibit similar trends as the cooling flow rate increases.

Specific observations include:

- Thinning of High Cpt Region Near the Hub: In the URANS case, as cooling flow increases, the high Cpt region near the hub progressively diminishes, indicating reduced total pressure losses in this area. In the experimental case, the high Cpt region is visible only in the zero cooling condition (MC = 0%). Under higher cooling flow conditions, this region becomes thinner and is not captured by the experimental sampling grid.
- Migration and Intensification of Loss Core: The loss core at lower radii, primarily caused by secondary flow effects near the hub, shifts to higher radii and intensifies in

magnitude. In the URANS case, its radial extent ranges from span = 24% to span = 37% for MC = 0%, whereas for MC = 2.7%, it extends from span = 28% to span = 41%. This is indicative of enhanced interaction between the cooling flow and the main flow, affecting secondary flow structures.

- Enlargement of Lower Channel Loss Core: An enlargement of the loss core on the right side in the bottom half of the channel is observed, suggesting the cooling flow's influence on secondary flow behavior in this region. In particular, in the URANS case, the tangential extent ranges from $\theta = 0.4$ to $\theta = 0.64$ for MC = 0%, whereas for MC = 2.7%, it extends from $\theta = 0.4$ to $\theta = 0.7$.

Figure 7a shows the normalized velocity distribution in the meridional plane for the two extreme cooling conditions: zero cooling and complete sealing. Data were extracted along the green plane (upstream of the vane) identified in Figure 2. In the hub region (span = 0–20%), the boundary layer thickness is higher in the case of complete sealing compared to the zero cooling condition. Figure 7b shows the radial velocity distribution in the meridional plane along the normalized axial direction (for cavity inlet section, shown in red) for the two extreme cooling conditions: zero cooling and complete sealing. In the sealing case (MC = 2.7%), the *Vr* value remains positive (indicating flow toward larger radii) across almost the entire axial direction, except for a small region near $z_{norm} = 1$, where *Vr* becomes slightly negative. Conversely, in the zero-cooling case, the *Vr* values are significantly lower throughout the axial direction, with notably negative values near $z_{norm} = 1$, indicating flow toward smaller radii. This is due to the fact that, in the zero cooling case, the boundary layer that developed in the portion of the main channel upstream of the cavity inlet is ingested into the cavity, whereas in the sealing case, this does not occur (Figure 7b), resulting in a thicker boundary layer at the leading edge of the blade (Figure 7a). This leads to increased losses in the sealing case, due to the development of more intense secondary flows at the hub, as will be demonstrated later.

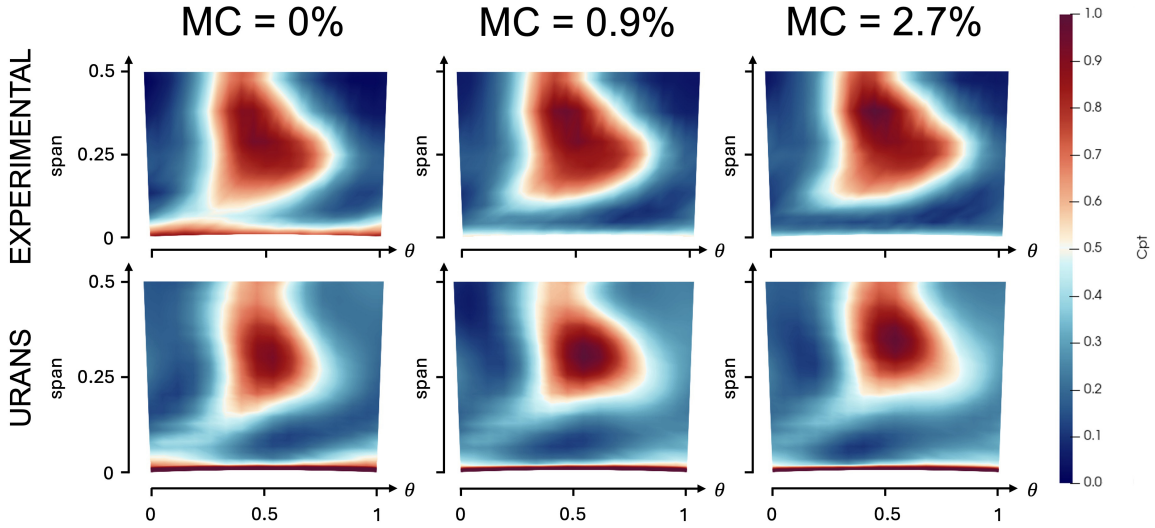


Figure 6. Normalized total pressure coefficient C_{pt} distributions (from hub to midspan) for different cooling mass flow rates: experimental vs. URANS results. The diagrams on the right-hand side (MC = 2.7%) correspond to the case of complete sealing.

To identify the unsteady effects associated with the cavity flow and assess their interaction with both the main flow and the unsteady phenomena induced by the upstream and downstream rotor bars, comparisons of instantaneous quantities are presented in Figure 8. The analysis is carried out at two distinct time instants, corresponding to two equally spaced positions of the rotor bars at 0% and 50% of the vane pitch. Since

the influence of the cavity flow is primarily noticeable at the cavity outlet [25–27], the results are shown for section (N. 1), as indicated in Figure 2. In Figure 8, it is also possible to see the position of the downstream rotor bars.

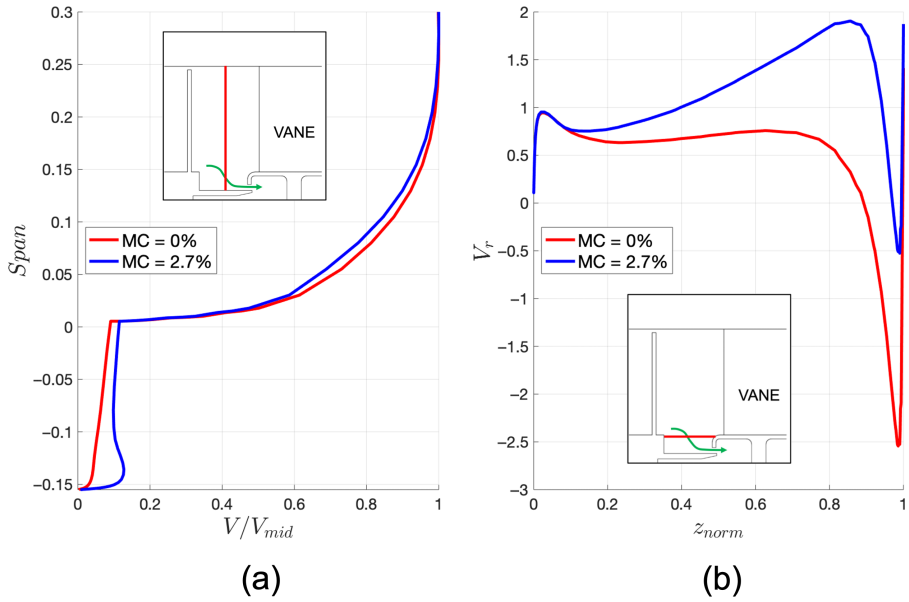


Figure 7. (**a**) Spanwise normalized velocity distribution and (**b**) axial *Vr* distribution under the two extreme cooling conditions: zero cooling (red) and complete sealing (blue).

We start by analyzing the flow angle, shown in Figure 8a. Notably, the circumferential periodicity of the flow exiting the cavity remains synchronized with the positions of the downstream rotor bars (red high flow angle region at midspan), emphasizing that the local behavior of this flow is strongly influenced by the potential field generated by the downstream bars. Additionally, the cavity flow itself is affected by the rotor bar positions, as indicated by the reduced radial extent of the negative flow deviation (overturning) in alignment with the rotor bars (dark blue low flow angle region, close to span = 0%). As the cooling flow rate increases, a distinct region of flow underturning emerges in the lower part of the channel (red high flow angle region close to the hub), positioned above the negative-angle flow strip associated with the cavity flow. This region extends across the entire tangential domain. The formation of this area is linked to the upstream hub boundary layer, which, under the complete sealing condition (MC = 2.7%), remains confined within the main channel. This alters the local flow angle and intensifies the secondary flow effects in this region.

Regarding the velocity magnitude shown in Figure 8b, the primary difference lies in the thickness of the low-velocity region (blue area) near the hub. The cavity flow is influenced by the rotor bar positions, as evidenced by the reduced radial extent of the velocity aligned with the rotor bars, resulting from their blocking effect. As the cooling flow rate increases, the low-velocity region becomes thicker. This is attributed to the hub boundary layer, which, under the complete sealing condition (MC = 2.7%), is not ingested into the cavity inlet and instead remains in the main channel. Consequently, the hub boundary layer thickens, as observed in Figure 7a, intensifying secondary flow effects in this region.

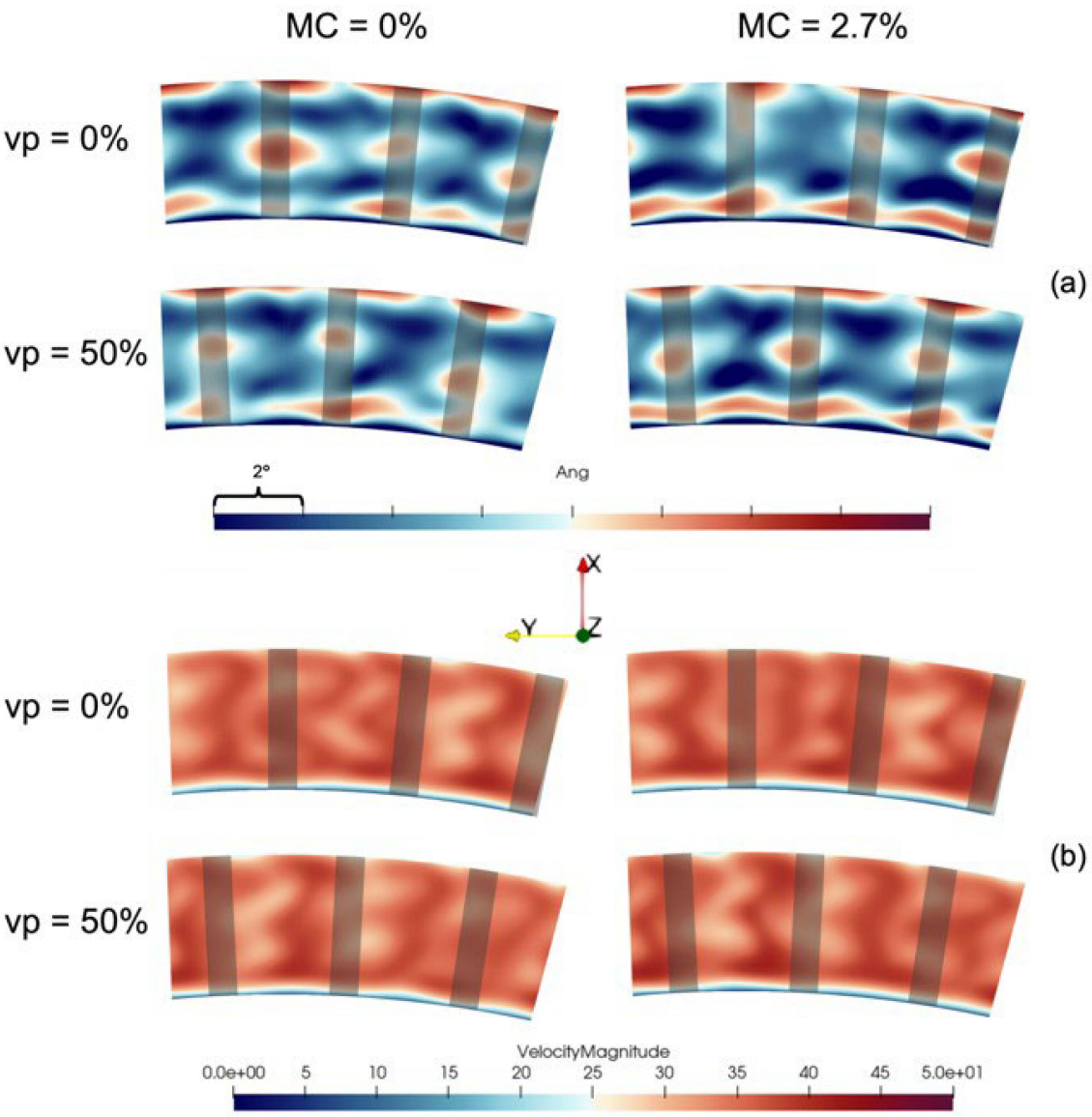


Figure 8. Contour plots of the flow angle (**a**) and velocity magnitude (**b**) downstream of the cavity outlet for the two cooling conditions, showing their variation over time.

Figure 9 shows the Q-criterion visualization in the vane passage for the two extreme cooling conditions: zero cooling and complete sealing. The cavity outlet surface is represented by the V_r contour plot (see Figure 9a,b). By comparing the two cooling flow rate conditions, we can see that in the shroud region, there are no differences and there is a similar development of the secondary flows. This is due to the fact that the loss core in the upper part of the channel appears unaffected by variations in cooling flow rates, highlighting a localized impact of the cooling flow near the hub and mid-span regions. Instead, in the hub region, it is possible to see much more intense secondary flows in the sealing condition (on the right). In fact, the sealing condition reveals a more intense passage vortex (in red), which interacts more strongly with the wake generated at the stator hub. This interaction produces a secondary trailing edge shed vortex (in blue) that is more intense compared to the zero cooling case, in agreement with the work of Schadler et al. [19]. This can be attributed to two factors. The first is the presence of a thicker boundary layer in the hub region under the sealing condition, as shown in Figure 7. A thicker boundary layer enhances secondary flows, leading to increased losses. The second factor is the higher radial

velocity values observed upstream of the stator leading edge, which will be examined in greater detail below.

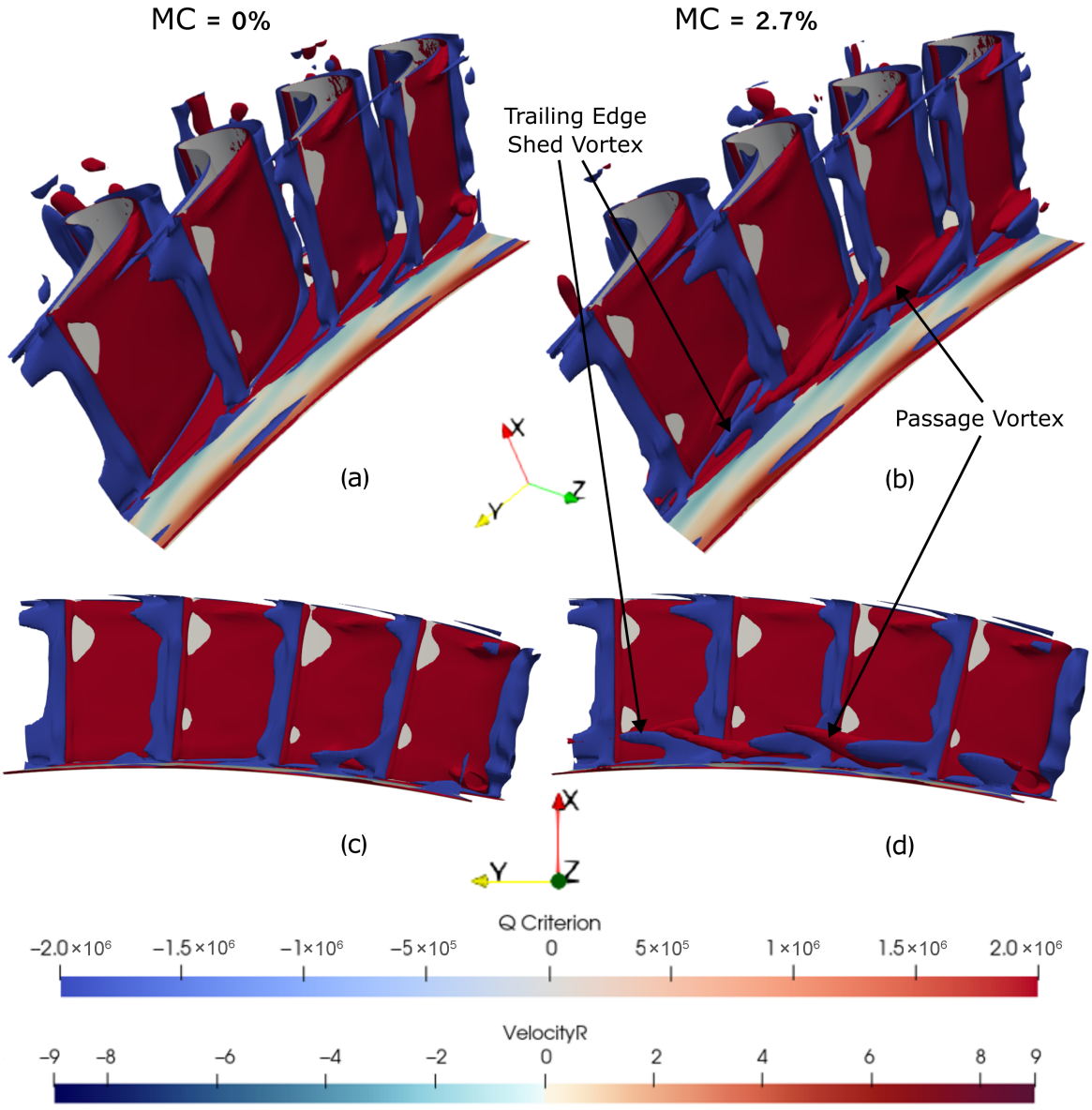


Figure 9. Q-criterion visualization in the vane passage under the two extreme cooling conditions: zero cooling (on the left) and complete sealing (on the right). (**a**,**b**) 3D view, (**c**,**d**) r-θ plane view.

Figure 10 shows the time-varying radial velocity distributions in the cavity inlet and cavity outlet sections for the two extreme cooling conditions: zero cooling and complete sealing. The visualization of the Q-criterion inside the vane passage is also shown. By comparing the two cooling flow rate conditions, we can see that in the cavity inlet section, there is a larger area with negative values of V_r (flow goes to lower radii) in the zero cooling condition. Instead, in the complete sealing condition, there is a larger area with positive values of V_r (flow goes to higher radii). This is due to the cooling flow rate injected into the cavity that prevents the ingress of the main flow inside the cavity. In the cavity outlet section, the V_r distribution is similar under both conditions, with positive V_r core regions located upstream of the rotor bar. These core regions align circumferentially with the rotor passage, separated by lower V_r regions corresponding to the rotating bars. This pattern arises from the potential effects induced by the rotor's leading edge. The main distinction

between the two cooling conditions lies in the magnitude of the positive V_r core regions, which exhibit higher values in the sealing case (right-hand side). This difference arises from the stronger interaction between the cavity flow and the main flow. In both cooling conditions, the cavity flow maintains the same $\dot{m}_{leak}$ value. However, in the zero cooling case, a portion of the main flow enters the cavity, reducing the mass flow rate passing through the vane compared to the rig inlet mass flow rate. Conversely, in the sealing case, $\dot{m}_{leak}$ is entirely supplied by the cooling mass flow rate injected into the cavity, ensuring that the entire rig inlet mass flow rate traverses the vane without any ingress into the cavity inlet.

In Figure 11, the circumferential trend of radial velocity in sections A, B, and C are shown. The locations of the three sections are indicated by the green lines in Figure 10 (see zero cooling case at 0% of the vane pitch). For each section in Figure 11, a comparison is made between the zero cooling case and the complete sealing case at two time instants.

In section A (upstream of the stator leading edge), it can be observed that the peak values of V_r increase with higher cooling flow rates, with the peak occurring at the vane passage, as shown in Figure 10. The effect of higher values of V_r is the generation of more intense passage vortices that develop at higher radii within the passage. They also exhibit a stronger interaction with the vane wake, leading to the generation of more intense trailing edge shed vortices, as seen in Figure 9. Comparing the curves at different time instants shows that they overlap, because the section A is located upstream of the stator and is not affected by rotating effects.

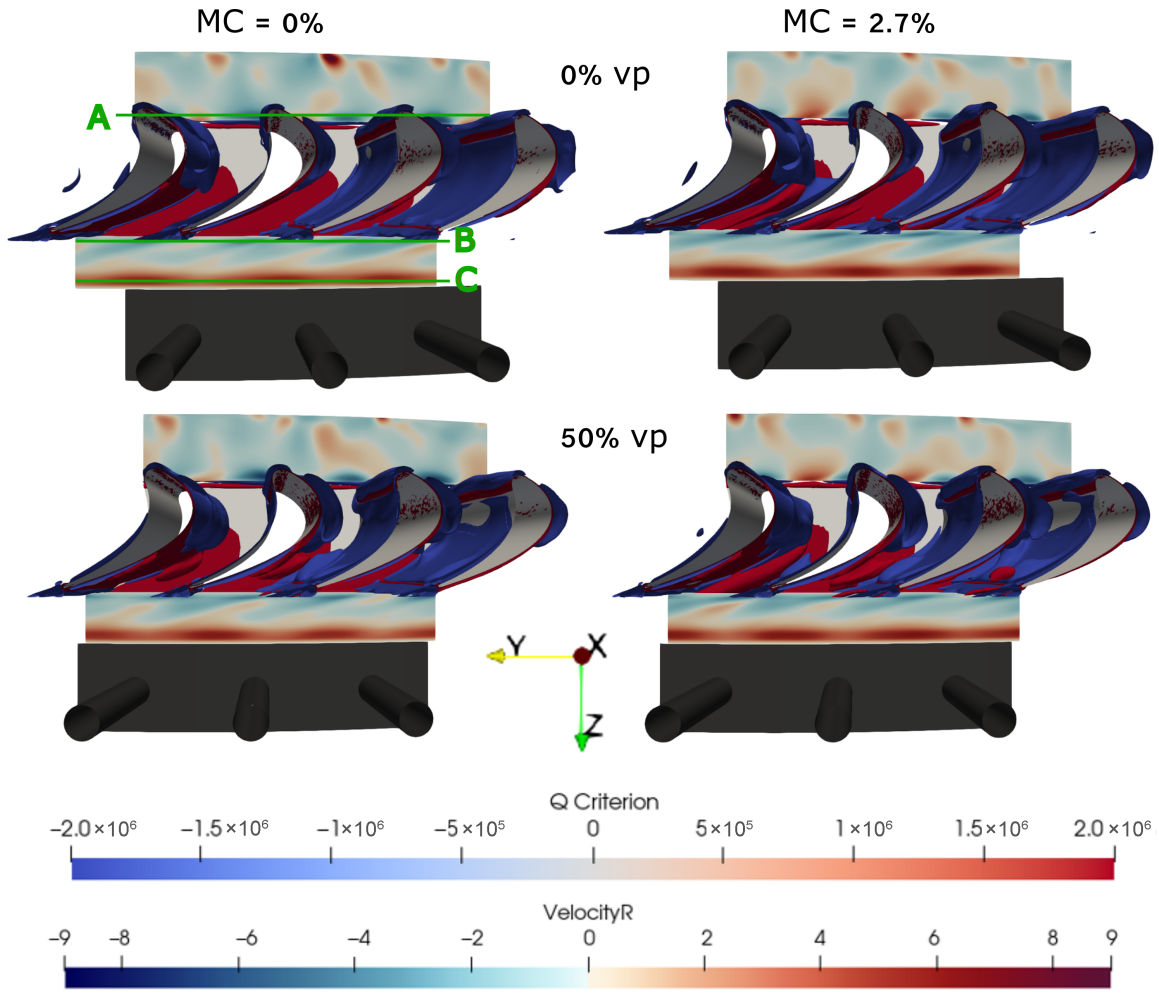


Figure 10. Contours of radial velocity for cavity inlet and cavity outlet sections under the two extreme cooling conditions: zero cooling (on the left) and complete sealing (on the right)—two time instances.

In section B (downstream of the stator trailing edge), it can be observed that the peaks of V_r occur at the same tangential positions for both the cooling condition and at both considered time instants, due to the proximity of the vanes and the absence of rotor-induced potential effects. The fluctuation in the peak values is attributed to the unsteadiness at the vane trailing edge.

In section C (upstream of the rotor leading edge), it can be observed that the peak values of V_r increase with higher cooling flow rates, with the peak occurring at the rotor bar passage, as shown in Figure 10. The effect of higher V_r values is a more intense interaction between the main flow and the flow exiting from the cavity outlet section. Comparing the curves at different time instants reveals a tangential shift, as section C is located upstream of the rotor and is influenced by the rotor's potential effects.

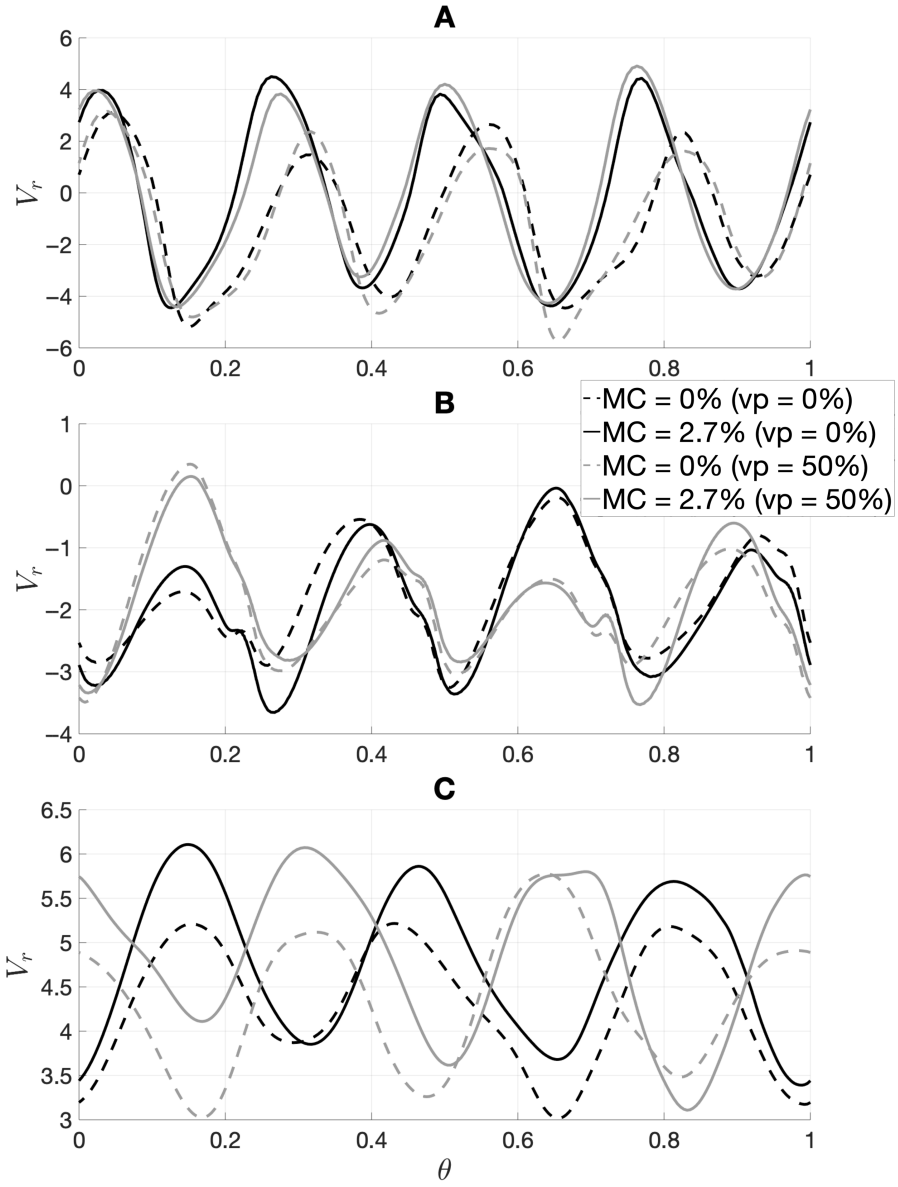


Figure 11. Circumferential trend of the radial velocity in sections (**A**) (upstream of the stator leading edge), (**B**) (downstream of the stator trailing edge), and (**C**) (upstream of the rotor leading edge). For each section, a comparison is made between the zero cooling case (dotted lines) and the complete sealing case (continuous lines) at two time instants.

Figure 12 presents the radial velocity distributions at the cavity inlet and outlet sections for two radial positions, $h1$ and $h2$, under the two extreme cooling conditions: zero cooling

and complete sealing. The visualization of the Q-criterion inside the vane passage is also shown. In the cavity inlet section, a similar behavior is observed for the two radial positions, $h1$ and $h2$. Under the zero cooling condition, a larger area exhibits negative V_r values, whereas under the complete sealing condition, a larger area displays positive V_r values, as seen in Figure 10. In the cavity outlet section, a significant difference is observed between the two radial positions. At section $h1$, the behavior aligns with the trend described in Figure 10, characterized by positive V_r core regions upstream of the rotor bars. Conversely, at section $h2$, there is a diffusion of V_r, with predominantly positive values across the section except within the stator wake regions downstream of the stator vane, where V_r becomes negative. Comparing the two cooling flow rate conditions at section $h2$, it can be observed that in the stator wake region, the negative V_r values are more intense (i.e., they have a higher incoming value) in the case of complete sealing. This is the hub passage vortex effect, which becomes more intense as the cooling flow rate injected into the cavity increases. This further demonstrates that the interaction between the cavity flow and the main flow has predominantly localized effects near the hub.

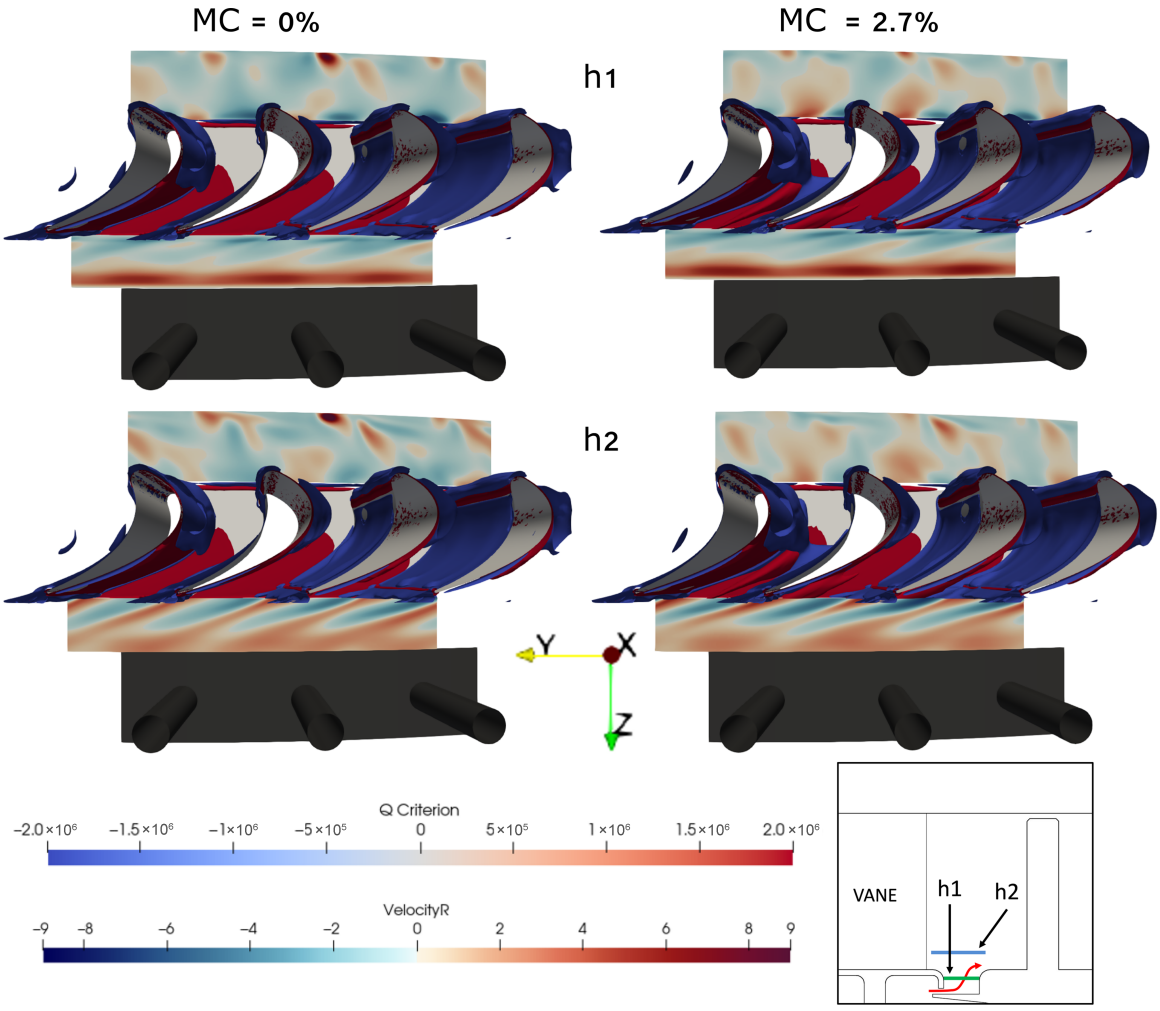


Figure 12. Contours of radial velocity for cavity inlet and cavity outlet sections for two radial positions, $h1$ (span = 0%) and h_2 (span = 8.3%), under the two extreme cooling conditions: zero cooling (on the left) and complete sealing (on the right).

4. Conclusions

This study investigated the impact of varying cooling flow rates on vane performance, focusing on the interaction between the cavity flow and the main flow. A combined analysis of experimental and numerical data validated the CFD procedure, revealing consistent

trends across varying cooling conditions. URANS predictions and experimental data showed that increasing the cooling flow reduces the high total pressure loss region near the hub. However, this also intensifies the loss core at higher radii due to enhanced interaction between the cooling and main flows. The complete sealing condition leads to a thicker boundary layer at the hub and higher radial velocity values upstream of the vane leading edge, resulting in stronger secondary flows and increased losses compared to the zero cooling case. The cavity inlet and outlet sections demonstrated distinct velocity distributions. The zero cooling condition exhibited more negative radial velocity V_r regions at the inlet, whereas the sealing condition had larger positive V_r regions, driven by the cooling flow rate injected into the cavity. The interaction between cavity flow and main flow primarily affects regions close to the hub, with minimal differences observed far from the hub region.

The present numerical approach, based on URANS simulations, provides valuable insights into the unsteady interactions between cavity and main flow. However, it inherently relies on turbulence modeling assumptions, which may limit its ability to fully capture small-scale vortex structures and transitional effects. High-fidelity approaches, such as LES methods, could offer a more detailed resolution of the flow physics at the cost of significantly increased computational expense. Future research should focus on extending the numerical analysis to include such advanced modeling techniques, allowing for a deeper understanding of secondary flow interactions and loss mechanisms. The impact of different operating conditions, such as varying rotational speeds and inlet turbulence levels, should be explored to enhance the applicability of the findings to real gas turbine configurations.

In conclusion, the findings highlight the significant influence of cooling flow dynamics on vane performance, emphasizing the need for precise control of cooling flows to optimize turbine efficiency. Understanding these interactions is critical for designing low-pressure turbines that achieve the desired balance between cooling effectiveness and aerodynamic performance.

Author Contributions: Conceptualization, D.B. (Daniele Biassoni), D.B. (Dario Barsi) and D.L.; methodology, D.B. (Daniele Biassoni) and D.B. (Dario Barsi); investigation, D.B. (Daniele Biassoni) and D.B. (Dario Barsi); data curation and visualization, D.B. (Daniele Biassoni); writing—original draft preparation, D.B. (Daniele Biassoni) and D.B. (Dario Barsi); writing—review and editing, D.L.; supervision, D.L.; funding acquisition, D.L. All authors have read and agreed to the published version of the manuscript.

Funding: This research was funded by the PRIN 2022 Project INERTIA (Ingress aNd Egress thRough Turbine rIm seAls) approved by the Italian Ministry of University, started in September 2023 (Project ID 20229FK9A9).

Data Availability Statement: Data are available on resonable request.

Acknowledgments: We acknowledge the CINECA award under the ISCRA initiative, for the availability of high-performance computing resources and support.

Conflicts of Interest: The authors declare no conflicts of interest.

Nomenclature

The following symbols and abbreviations are used in this manuscript:

Roman letters

C_x	Axial chord [m]
C_{pt}	Total pressure coefficient $= \frac{p_{t1}(r,y)-p_{t2}(r,y)}{0.5\rho v^2_{2,id}}$
$\dot{m}_{cool}$	Cooling mass flow rate [kg s^{-1}]

$\dot{m}_{FP}$	Flow path mass flow rate [kg s^{-1}]
k	Turbulent kinetic energy [m^2 s^{-2}]
$\dot{m}_{leak}$	Leakage mass flow rate [kg s^{-1}]
$\dot{m}_{rim}$	Rim mass flow rate [kg s^{-1}]
y^+	Dimensionless wall distance [-]
p	Pressure [Pa]
R	Radial coordinate [m]
V	Velocity [m s^{-1}]
vp	Vane pitch [-]
z	Axial coordinate [m]
MC	Percentage ratio of cooling flow rate to main channel flow rate [-]
Greek letters	
ϵ	Turbulent dissipation rate [m^2 s^{-3}]
ρ	Density [kg m^{-3}]
Acronyms and abbreviations	
CFD	Computational Fluid Dynamics
CS	Cooling slot
FP	Flow path
LES	Large Eddy Simulation
LPT	Low-Pressure Turbine
$URANS$	Unsteady Reynolds-Averaged Navier–Stokes
Superscripts and subscripts	
1	Inlet vane section value
2	Outlet vane section value
id	Ideal
max	Maximum
mid	Midspan
$norm$	Normalized
r	Radial
t	Total/stagnation value

References

1. Moore, A. Gas turbine engine internal air systems: A review of the requirements and the problems. *Turbo Expo Power Land Sea Air* **1975**, *80005*, V001T01A001.
2. Johnson, B.V.; Mack, G.J.; Paolillo, R.E.; Daniels, W.A. *Turbine Rim Seal Path Flow Ingestion Mechanisms*; AIAA Paper 94; AIAA: Reston, VA, USA, 1994.
3. Chew, J.; Gao, F.; Palermo, D. Flow mechanisms in axial turbine rim sealing. *Proc. Inst. Mech. Eng. Part C J. Mech. Eng. Sci.* **2018**, *233*, 7637–7657. [CrossRef]
4. Schrewe, S.; Werschnik, H.; Schiffer, H.P. Experimental analysis of the interaction between rim seal and main annulus flow in a low pressure two stage axial turbine. *J. Turbomach.* **2013**, *135*, 051003. [CrossRef]
5. Ong, J.H.; Miller, R.J.; Uchida, S. The effect of coolant injection on the endwall flow of a high pressure turbine. *Turbo Expo Power Land Sea Air* **2006**, *4241*, 915–924.
6. Zerobin, S.; Peters, A.; Bauinger, S.; Ramesh, A.; Steiner, M.; Heitmeir, F.; Göttlich, E. The behavior of turbine center frames under the presence of purge flows. *Turbo Expo Power Land Sea Air* **2017**, *50787*, V02AT40A012.
7. Sterzinger, P.Z.; Zerobin, S.; Merli, F.; Wiesinger, L.; Peters, A.; Maini, G.; Dellacasagrande, M.; Heitmeir, F.; Göttlich, E. Impact of varying high-and low-pressure turbine purge flows on a turbine center frame and low-pressure turbine system. *J. Turbomach.* **2020**, *142*, 101011. [CrossRef]
8. Schuepbach, P.; Abhari, R.S.; Rose, M.; Germain, T.; Raab, I.; Gier, J. Effects of suction and injection purge-flow on the secondary flow structures of a high-work turbine. *J. Turbomach.* **2010**, *132*, 021021. [CrossRef]
9. Chilla, M.; Hodson, H.; Newman, D. Unsteady interaction between annulus and turbine rim seal flows. *J. Turbomach.* **2013**, *135*, 051024. [CrossRef]
10. Jackson, R.; Christodoulou, L.; Li, Z.; Sangan, C.M.; Ambrose, S.; Jefferson-Loveday, R.; Lock, G.D.; Scobie, J.A. Influence of swirl and ingress on windage losses in a low-pressure turbine stator-well cavity. *Exp. Fluids* **2023**, *64*, 173. [CrossRef]

11. Jackson, R.W.; Li, Z.; Christodoulou, L.; Ambrose, S.; Sangan, C.M.; Jefferson-Loveday, R.; Lock, G.D.; Scobie, J.A. Windage Torque Reduction in Low-Pressure Turbine Cavities Part II: Experimental and Numerical Results. *J. Turbomach.* **2024**, *146*, 061005. [CrossRef]
12. Orsini, L.; Picchi, A.; Bonini, A.; Innocenti, L.; Di Benedetto, D.; Da Soghe, R.; Mazzei, L. Design Procedure of a Rotating Cavity Rig for Hot Gas Ingestion Investigation. *Turbo Expo Power Land Sea Air* **2022**, *86045*, V06BT14A011.
13. Orsini, L.; Picchi, A.; Facchini, B.; Bonini, A.; Innocenti, L. On the use of PSP to Determine the Rim Sealing Effectiveness. *Turbo Expo Power Land Sea Air* **2023**, *87011*, V07BT14A022.
14. Orsini, L.; Picchi, A.; Facchini, B.; Bonini, A.; Innocenti, L. Impact of the Purge Flow Density Ratio on the Rim Sealing Effectivemess in Hot Gas Ingestion Measurements. *J. Turbomach.* **2023**, *146*, 021002. [CrossRef]
15. Cao, C.; Chew, J.W.; Millington, P.R.; Hogg, S.I. Interaction of Rim Seal and Annulus Flows in an Axial Flow Turbine. *J. Eng. Gas Turbines Power* **2004**, *126*, 786–793. [CrossRef]
16. Roy, R.; Feng, J.; Narzary, D.; Saurabh, P.; Paolillo, R. Experiments on Gas Ingestion Through Axial-Flow Turbine Rim Seals. *Turbo Expo Power Land Sea Air* **2004**, *41693*, 347–358.
17. Beard, P.; Gao, F.; Chana, K.; Chew, J. Unsteady flow phenomena in turbine rim seals. *J. Eng. Gas Turbine Power* **2016**, *139*, 032501. [CrossRef]
18. Savov, S.; Atkins, N.; Uchida, S. Comparison of single and double lip rim seal geometry. *Turbo Expo Power Land Sea Air* **2016**, *49781*, V05AT15A003.
19. Schädler, R.; Kalfas, A.; Abhari, R.; Schmid, G.; Voelker, S. Modulation and radial migration of turbine hub cavity modes by the rim seal purge flow. *J. Turbomach.* **2017**, *139*, 011011. [CrossRef]
20. Town, J.; Averbach, M.; Camci, C. Experimental and Numerical Investigation of Unsteady Structures within the Rim Seal Cavity in the Presence of Purge Mass Flow. *Turbo Expo Power Land Sea Air* **2016**, *49705*, V02BT38A018.
21. Revert, A.B.; Beard, P.F.; Chew, J. Flow and ingestion in a turbine disc cavity under rotationally-dominated conditions. *Int. J. Turbomach. Propuls. Power* **2021**, *6*, 29. [CrossRef]
22. Hu, B.; Yao, Y.; Wang, M.; Wang, C.; Liu, Y. Flow and performance of the disk cavity of a marine gas turbine at varying nozzle pressure and low rotation speeds: A numerical investigation. *Machines* **2023**, *11*, 68. [CrossRef]
23. Guida, R.; Lengani, D.; Simoni, D.; Ubaldi, M.; Zunino, P. New facility setup for the investigation of cooling flow, viscous and rotational effects on the interstage seal flow behavior of a gas turbine. *Turbo Expo Power Land Sea Air* **2018**, *51098*, V05BT15A017.
24. Barsi, D.; Costa, C.; Lengani, D.; Simoni, D.; Venturino, G.; Zunino, P. Experimental and Numerical Analysis of Cavity/Mean-Flow Interaction in Low Pressure Axial Flow Turbines. *J. Therm. Sci.* **2021**, *30*, 2178–2185. [CrossRef]
25. Barsi, D.; Lengani, D.; Simoni, D.; Venturino, G.; Bertini, F.; Giovannini, M.; Rubechini, F. Analysis of the Loss Production Mechanism Due to Cavity–Main Flow Interaction in a Low-Pressure Turbine Stage. *J. Turbomach.* **2022**, *144*, 091004. [CrossRef]
26. Barsi, D.; Lengani, D.; Simoni, D.; Bertini, F.; Giovannini, M.; Rubechini, F. Analysis of the Sealing Flow Rate on Loss Production Mechanisms in LPT Stage. In Proceedings of the 15th European Conference on Turbomachinery Fluid Dynamics and Thermodynamics, Budapest, Hungary, 24–28 April 2023.
27. Barsi, D.; Biassoni, D.; Lengani, D.; Simoni, D.; Ubaldi, M. Sealing Flow Rate Effects on Unsteady Loss Production in a Low Pressure Turbine Stage. *Turbo Expo Power Land Sea Air* **2024**, *88063*, V12BT30A042.
28. Opoka, M.M.; Hodson, H.P. Transition on the T106 LP Turbine Blade in the Presence of Moving Upstream Wakes and Downstream Potential Fields. *J. Turbomach.* **2008**, *130*, 041017. [CrossRef]
29. CADENCE. *FINE/Turbo User Manual*; CADENCE: San Jose, CA, USA, 2023
30. Jameson, A.; Baker, T. Multigrid solution of the Euler equations for aircraft configurations. In Proceedings of the 22nd Aerospace Sciences Meeting, Reno, NV, USA, 9–12 January 1984; p. 93.
31. Mavriplis, D.; Jameson, A. Multigrid solution of the Euler equations on unstructured and adaptive meshes. In *Multigrid Methods*; CRC Press: Boca Raton, FL, USA, 2020; pp. 413–430.

Disclaimer/Publisher's Note: The statements, opinions and data contained in all publications are solely those of the individual author(s) and contributor(s) and not of MDPI and/or the editor(s). MDPI and/or the editor(s) disclaim responsibility for any injury to people or property resulting from any ideas, methods, instructions or products referred to in the content.